Textured Na<inf>2</inf>V<inf>6</inf>O<inf>16</inf>·3H<inf>2</inf>O Cathode Tuned via Crystal Engineering Endows Aqueous Zn-Ion Batteries

ACS Energy LETTERS

http://pubs.acs.org/journal/aelccp

Textured $Na_2V_6O_{16}·3H_2O$ Cathode Tuned via Crystal Engineering Endows Aqueous Zn-Ion Batteries with High Rate Capability and Adequate Lifespan

Shijia Li, Xieyu Xu, Kai Wang, Weixin Chen, Xia Lu, Zhongxiao Song, Jang-Yeon Hwang, Jaekook Kim, Ying Bai,* Yangyang Liu,* and Shizhao Xiong*

Cite This: *ACS Energy Lett.* 2022, 7, 3770−3779

Read Online

ACCESS | Metrics & More | Article Recommendations | Supporting Information

ABSTRACT: **Aqueous zinc-ion batteries (ZIBs) play a vital role in large-scale energy storage for smart grids due to their environmental friendliness, safety, and low cost. Unfortunately, the application of ZIBs has been challenged by the relatively low capacity of cathode materials, especially at higher rates, which originates from the sluggish diffusion of Zn ions. Herein, a crystal engineering strategy is explored for using bernesite, $Na_2V_6O_{16}·3H_2O$ (NVO), for regulating the diffusion-preferable texture, which was beneficial for fostering Zn ions' diffusion and thus guaranteeing a uniform concentration inside the cathode. An enlarged capacity at a higher rate was obtained, delivering a capacity of 156.9 mAh g^{-1} at the ultra-high current density of 20 A g^{-1}, of which 140.6 mAh g^{-1} remained after 5000 cycles. The use of crystal engineering to regulate the texture of cathode materials paves the way to boost the application of NVO in aqueous ZIBs, which could be translated to design state-of-the-art cathodes for other battery systems.**

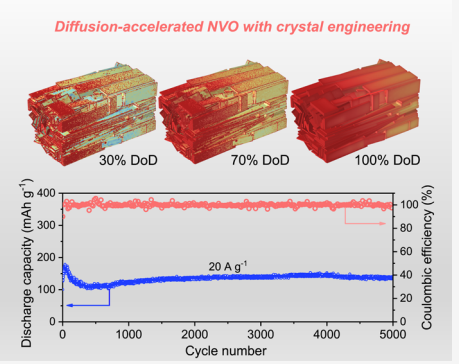

To date, the energy storage market related to portable consumer electronic devices as well as electronic vehicles has been dominated by lithium-ion batteries (LIBs) containing a graphite anode with liquid organic electrolytes, which deliver satisfying energy density with outstanding cycling stability for the energy supply.[1−6] Despite the promising achievements already made, LIBs cannot meet the requirements of low cost and safety for the large-scale energy storage system needed for the smart grid, which is a vital part of "carbon neutrality".[7−9] In contrast to the high cost for a limited lithium recourse and safety hazards caused by the utilization of organic electrolyte and the dendrite deposition of lithium metal,[10,11] aqueous zinc-ion batteries (AZIBs) have been called the "holy grail" candidates for improved safety, environmental friendliness, and low cost, as well as facile manufacturing processes. The merits of zinc metal include a high theoretical capacity of 820 mAh g^{-1}, the low redox potential of −0.76 V vs standard hydrogen electrode, and great element abundance.[12−15]

Nevertheless, the large-scale application of ZIBs in smart grids is mainly hindered by cathode materials that deliver relatively low capacity.[16,17] Since alpha-manganese-dioxide (α-MnO_2) was reported by Kang et al. a decade ago,[18] polymorphous MnO_2,[19−22] Prussian blue analogs,[23−25] as well as vanadium-based materials[26,27] have been subsequently explored as cathode materials for ZIBs. Vanadium-based materials are expected to exhibit higher capacity with excellent stability for commercialization of ZIBs due to the variable valences, ranging from +5 to +2, and the open skeleton with the changeable structure for the V−O coordination polyhedron.[28,29] As a typical representative of vanadium-based materials, sodium vanadate stands out from the crowd with its diverse crystal structures and excellent electrochemical properties.[30] In particular, barnesite, $Na_2V_6O_{16}·3H_2O$ (NVO), which has been widely used for LIBs as well as sodium-ion batteries,[31,32] is a typical layer-structure material for ZIBs comprised of V_3O_8, wherein interstitial hydrated sodium ions act as pillars between layers to stabilize the crystal

Received: August 22, 2022
Accepted: September 30, 2022

structure.[33,34] Although the application of NVO materials for ZIBs has been pioneered by Kim and co-workers,[35] a guideline for improving the electrochemical performance of NVO in ZIBs is still missing, slowing down the commercial progress of ZIBs with NVO cathode in large-scale energy storage systems.

Generally, NVO, a member of the Hewettite family ($M_2V_6O_{16}{\cdot}nH_2O$, where M = monovalent element), is indexed to a pure monoclinic crystal phase with a space group of $P2_1/m$. Like most crystal cathode materials,[36,37] the migration of Zn ions inside the NVO cathode is governed by the specific texture. As illustrated in Figure 1, the layer of NVO is

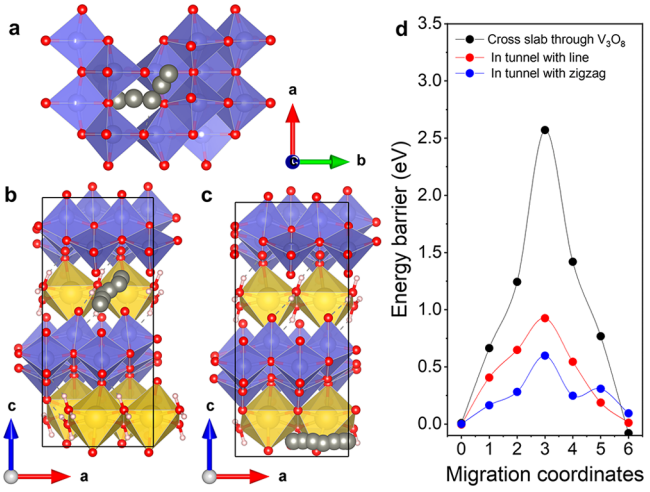

Figure 1. Diffusion of Zn ions inside the $Na_2V_6O_{16}{\cdot}3H_2O$ (a) across the V_3O_8 slab, (b) in the tunnel in a zigzag, and (c) in the tunnel in a line. (d) Diffusion energy barriers of Zn ions inside the layered NVO through different pathways.

structured with V_3O_8 coordinated by hydrated sodium ions. Thus, two migration pathways can be predicted, across the V_3O_8 layer and in the tunnel between V_3O_8 layers, which are in accordance with two different textured NVO cathodes, respectively. Moreover, sodium vanadate, with a stable tunnel structure, has good reversible insertion/extraction performance for Zn^{2+} without a phase transition.[38] Thus, tuning the texture of as-prepared NVO can regulate the diffusion of Zn ions inside the cathode, proposed as an effective path to enlarge the capacity and improve the cycling stability. Unfortunately, texturing the NVO using a suitable method to regulate the migration pathway for the diffusion of Zn ion inside has received little attention up to now.

Herein, crystal engineering is proposed to theoretically and experimentally regulate the specific texture of the NVO cathode and thus improve the electrochemical performance of the cathode material in AZIBs. First, the preferential migration pathway with a lower diffusion energy barrier was unrolled at the atomic level, guiding the synthesis of specifically textured NVO. Taking advantage of crystal engineering, excellent electrochemical performance, including the enlarged capacity with cycling stability as well as higher rate capability, was obtained. The electrochemical mechanism of the textured NVO cathode was intensively illustrated through the visualization of related electrochemical fields inside the electrode containing the textured NVO cathode. The strategy of crystal engineering in this work paves a promising avenue to fundamentally improve the electrochemical performance of cathode materials and foster the application of AZIBs.

First, the diffusion of Zn ions inside the NVO cathode was revealed atomically with the Density Function Theory on the Vienna *Ab initio* Simulation Package (see experimental details in the Supporting Information). $Na_2V_6O_{16}$, a kind of tunnel-type material with a space group of $P2_1/m$, is composed of a V_3O_8 layer with Na ions between layers,[39] in which the V_3O_8 layer is in an alternate arrangement of VO_5 pentahedrons and VO_6. The optimized stable structure is obtained by considering the occupied sites of various Na ions and crystal water molecules (Figures S1 and S2).[39] Similar to the six-coordinate environment of Na in NVO, the ZnO_6 octahedral environment is jointly formed by an oxygen in the V_3O_8 layer and that from a water molecular (Figure S3). As shown in Figure 1a–c and Figure S4, two possible pathways of Zn ions diffusion inside NVO are predicted: diffusion across the V_3O_8 layer and diffusion in the tunnel in a zigzag or in a line. Based on the high diffusion energy barrier up to 2.56 eV, the migration of Zn ions across the V_3O_8 layer is proved to happen rarely, illustrating that it is difficult for Zn ions to diffuse cross the V_3O_8 layer and enter the bulk phase when the material surface is dominated by the (001) crystal plane.[38] On the other hand, Zn ions can diffuse in a zigzag way and in a linear way from a specific Zn site to another one in the interlayer tunnel, which requires overcoming the energy barriers of 0.59 and 0.92 eV, respectively (Figure 1d). Furthermore, the diffusion of Zn ions in the tunnel is preferable to crossing the V_3O_8 layer. Experimentally, the surface of NVO, comprised of a V_3O_8 layer, is represented with a (001) crystal plane, which lacks the preferable diffusion pathway.[30] When b is not equal to 0 in the crystal plane (abc), such as (111), NVO is dominated by the exposed tunnels. There exists a high-speed diffusion pathway for Zn ions, which can be expected to show a greater diffusion coefficient for the Zn ions. Therefore, increasing the number of exposed tunnels with the specific crystal plane via crystal engineering is proposed as a fundamental approach to improve the electrochemical performance of NVO cathodes.

According to the aforementioned concept, crystal engineering of the textured NVO cathode can be expected to improve its electrochemical performance due to the predictable diffusion facilitated for Zn ions inside the NVO lattice along the (111) plane, which is closely governed by the synthetic process. As reported previously, hydrogen peroxide, a kind of environment-friendly oxidizer, can open the double bond between vanadium and oxygen to form a poly vanadium oxide chain. Thus, as shown in Figure 2a, hydrogen peroxide was selected as the synthetic regulator, where the amounts were set as 4, 6, 8, and 10 mL in a 50 mL solution. Then, sodium hydroxide was added to the solution of vanadium oxide for double-bond-opening. After being stirred for 2 h, the solution was transported into the Teflon liner and hydrothermally reacted at 200 °C for a day (see experimental details in the Supporting Information). The texture patterns of the as-prepared NVOs with 4, 6, 8, and 10 mL of hydrogen peroxide, named NVO-4, NVO-6, NVO-8, and NVO-10, were monitored by X-ray diffraction (XRD). The whole patterns are consistent with standard PDF#16-0601, showing a typical Hewettite structure with a space group of $P2_1/m$ (Figure 2b). Specifically, the texture index (TI) can be determined by quantitative analyses of the XRD peaks using the following equation:[40,41]

https://doi.org/10.1021/acsenergylett.2c01890
ACS Energy Lett. 2022, 7, 3770−3779

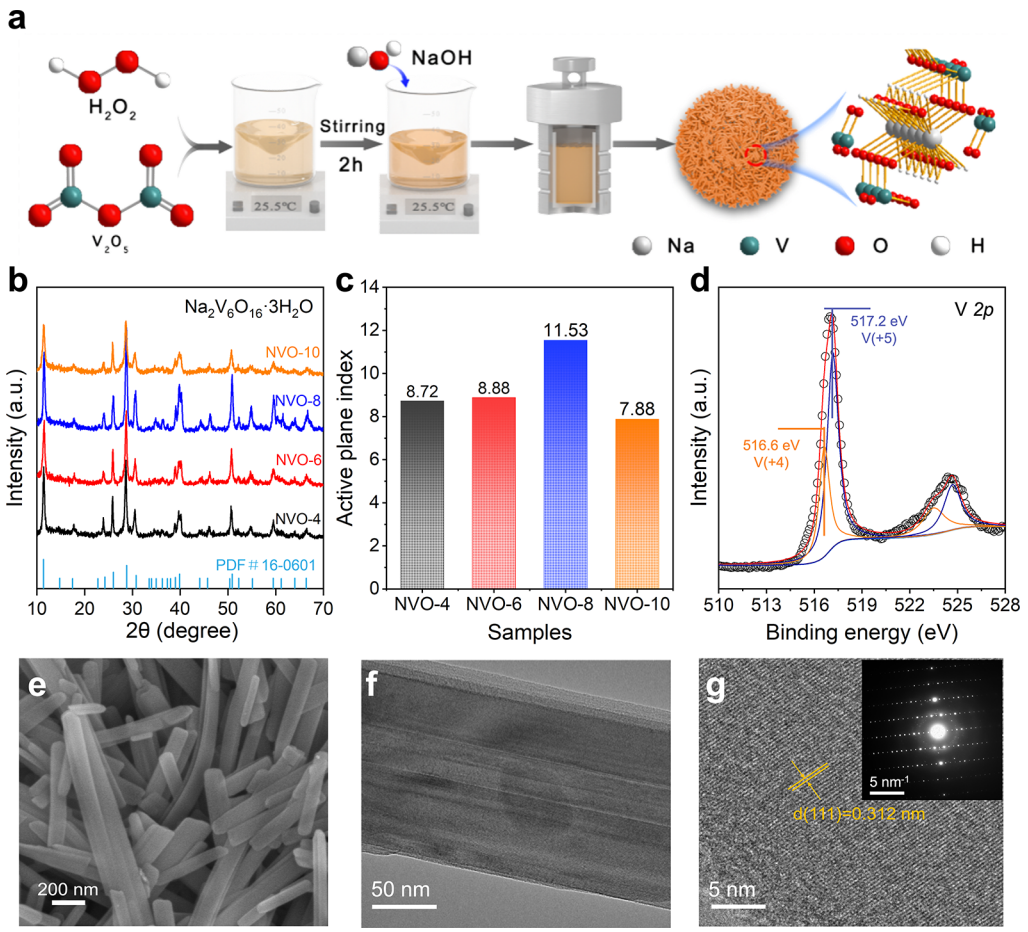

Figure 2. Synthesis of textured $Na_2V_6O_{16}·xH_2O$. (a) Schematic diagram of the synthesis process of textured NVO. (b) X-ray diffraction pattern of the as-prepared NVO samples and (c) corresponding active plane index. (d) X-ray photoelectron spectroscopy of V 2*p* with the as-prepared textured NVO. (e) Scanning electron microscopy image and (f, g) transmission electron microscopy images in (f) moderate magnification and (g) high magnification with the as-prepared textured NVO.

$$\mathrm{TI} = \frac{I_{hkl}/I^0_{hkl}}{\frac{1}{n}\sum (I_{hkl}/I^0_{hkl})} \quad (1)$$

where I_{hkl} and I^0_{hkl} are the integral intensities of the (*abc*) diffraction peaks for the as-prepared NVO and standard NVO (PDF#16-0601), respectively, and n is the number of diffraction peaks in the XRD patterns. Here, the ratio of the sum of the total active plane (*abc*) with $b \neq 0$ to the inactive plane (*abc*) with $b = 0$ is defined as the active plane index. As shown in Figure 2c, the index for the active plane rises with the increase of added hydrogen peroxide from 4 to 8 mL and then decreases when the amount added is 10 mL, predicting that the electrochemical performance can be optimized by using NVO-8. Notable weight losses of 4.9, 6.5, 7.5, and 4.8 wt%, respectively, for NVO-4, NVO-6, NVO-8, and NVO-10 at the temperature of 360 °C are revealed by thermogravimetric analysis (TGA), implying that 1.74, 2.34, 2.73, and 1.70 water molecules are adhered per unit stoichiometry (Figure S5).

X-ray photoelectron spectroscopy (XPS) was employed to investigate the chemical valences of each element in as-prepared NVO. Typically, textured NVO-8 consists of Na, V, and O in a ratio of 1:5.92:9.55 (Figure S6). The high-resolution XPS V $2p_{3/2}$ spectra of textured NVO-8 show two peaks at 516.6 and 517.2 eV, being characteristics of V(+4) and V(+5),[39,42] respectively (Figure 2d). Similarly, high-resolution XPS Na 1*s* and V 2*p* + O 1*s* spectra (Figure S7) proved the presence of Na and O elements. Meanwhile, the similar chemical valences of related elements in different NVOs are confirmed by XPS as well (Figure S8). This leaves no doubt that NVO with different textures is successfully synthesized in this work.

Furthermore, the morphologies of the as-prepared NVO were revealed with scanning electron microscopy (SEM) and the high-resolution transmission electron microscope (HRTEM). As shown in Figure 2e and Figure S9, the nanobelt morphologies of as-prepared NVOs are observed with an average width of 150 nm. Along with the increasing amount of added hydrogen peroxide from 4 to 8 mL, the length of the nanobelts increases. Yet, the obvious belt-like morphology disappears with an overaddition of hydrogen peroxide (10 mL). The morphology change with the increasing addition of hydrogen peroxide is reflected by the surface area. The measured surface areas initially increased gradually from 41.5 to 46.2 and then decreased to 36.9 $m^2\ g^{-1}$, respectively, with increasing concentration of H_2O_2 (Figure S10). Moreover, satisfying crystallinity of the as-prepared NVO-8 and the uniform distribution of related elements are confirmed by the HRTEM images in Figure 2f,g and element mapping in Figure S11. To sum up, the textured NVO-8 with a higher active plane index was successfully prepared by the regulation of added hydrogen peroxide, which was expected to enhance the electrochemical performance, especially the capacity and rate

https://doi.org/10.1021/acsenergylett.2c01890
ACS Energy Lett. 2022, 7, 3770−3779

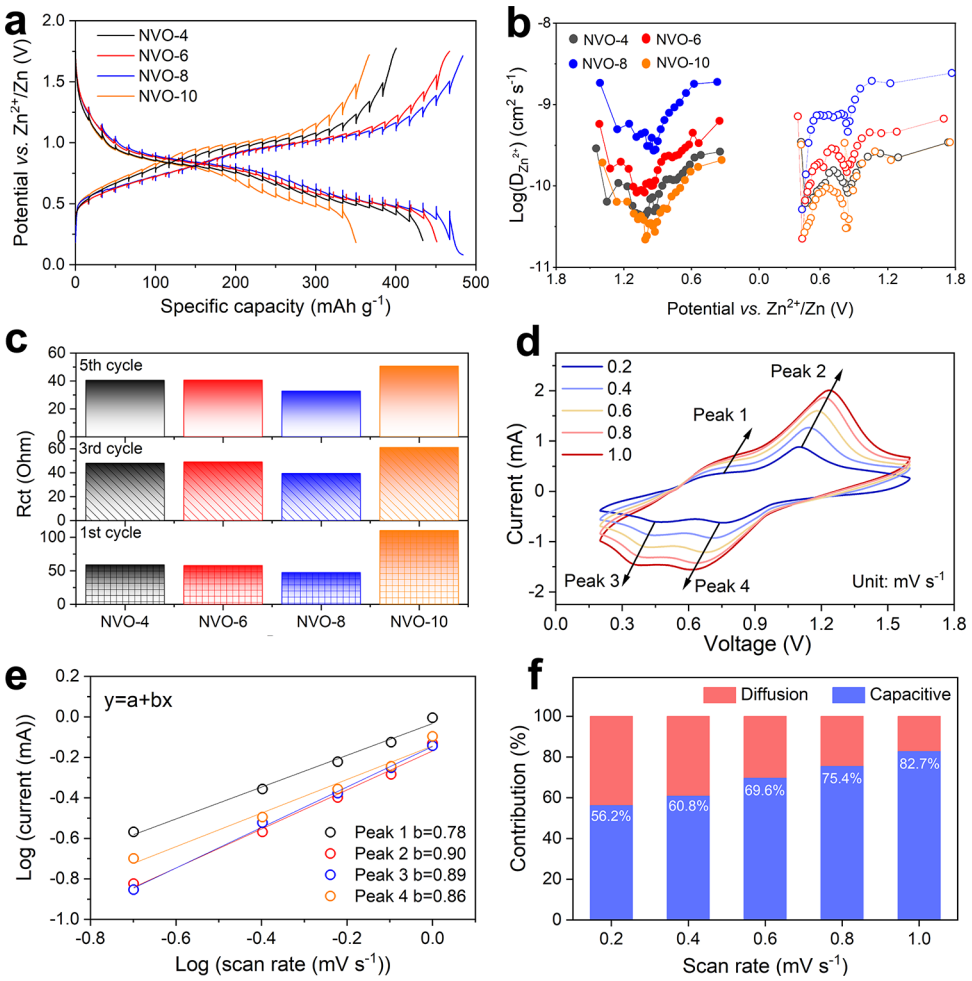

Figure 3. Kinetics of the textured NVO-8 cathode for AZIBs. (a) Galvanostatic intermittent titration technique (GITT) curve of different NVO cathodes and (b) corresponding diffusion coefficients of Zn ions on NVO cathodes. (c) Resistance for charge transfer of different NVO cathodes during a series of cycles. (d) Cyclic voltammetry curves of textured NVO cathode at different scanning rates ranging from 0.2 to 1.0 mV s^{-1}. Corresponding (e) relationship between peak currents and scan rates and (f) capacitive contributions of textured NVO at different scan rates.

performance, due to the reinforced diffusion of Zn ions inside the NVO-8 lattice gallery as cathode for AZIBs.

In general, as a kind of transient measurement method, the galvanostatic intermittent titration technique (GITT) was performed to reveal the relationship between the diffusion of zinc ions and the charge transfer for textured NVO-8 (see calculation details in the Supporting Information and Figure S12).[43] As shown in Figure 3a,b, the textured NVO-8 cathode demonstrates the highest diffusion coefficient. Specifically, during the discharge process, the diffusion coefficient of the NVO-8 cathode decreases to 5×10^{-9} cm^{-2} s^{-1} before 0.9 V and increases to 5×10^{-10} cm^{-2} s^{-1} at 0.3 V, which can be explained by the changing interlayer distance watershed by 0.9 V. Not only is the diffusion coefficient of Zn ions inside the textured NVO-8 lattice greater than those of other cathodes during discharge, but also it is the greatest one during the charge process. Also, the resistance for charge transfer (R_{ct}) of NVO cathodes was obtained using electrochemical impedance spectroscopy (EIS).[44] The NVO-8 cathode, with the highest active plane index, delivers the lowest resistance, which is consistent with the GITT results (Figure 3c). Therefore, the diffusion of Zn ions in textured NVO-8 is kinetically fastest in the synthesized samples.

Furthermore, the electrochemical kinetics of textured NVO-8 was studied using cyclic voltammetry (CV) scanned at a series of rates ranging from 0.2 to 1.0 mV s^{-1}. As shown in Figure 3d, the relative shift occurs along with the increase in scanning rate, which can be demonstrated by the occurrence of polarization along with the zincation and de-zincation. The relationship between peak current (i) and scan rate (v) could be described by the equation[38,45] $\log(i) = b \log(v) + \log(a)$, where a and b are adjustable parameters. After fitting the plots of peak current at different scanning rates, the slope b can be found to be $b = 0.78$, 0.9, 0.89, and 0.86 for peaks 1, 2, 3, and 4 in Figure 3e, respectively, illustrating that the storage of charge, i.e., Zn ions, was under the cumulative control of diffusion and capacitive behavior. Meanwhile, the ratio of the contributions of capacitive behavior and diffusion control can be obtained by using the equation[46−48] $i = k_1\nu + k_2\nu^{1/2}$.The capacitance proportion was thus determined to be elevated from 56.2 to 82.7% when increasing the scan rate from 0.2 to 1.0 mV s^{-1} (Figure 3f), suggesting that the reaction of textured NVO-8 at a high scan rate is largely controlled by surface capacitive behavior.

As mentioned before, the special texture of the NVO cathode tuned by the amount of synthetic regulator of

https://doi.org/10.1021/acsenergylett.2c01890
ACS Energy Lett. 2022, 7, 3770−3779

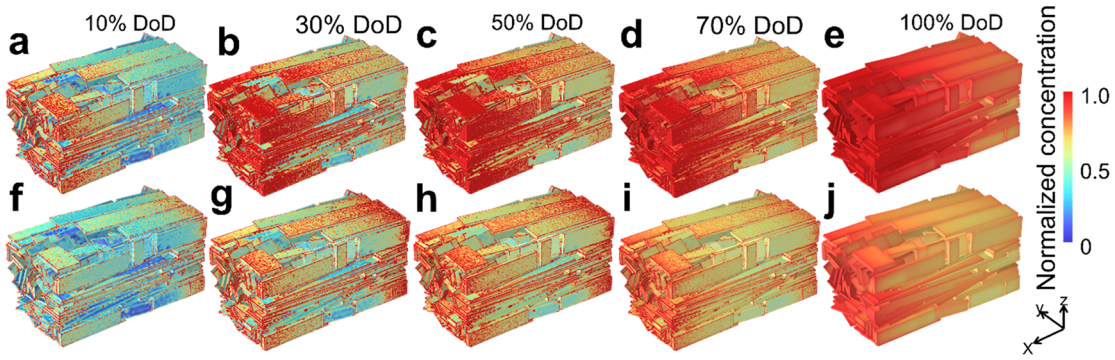

Figure 4. Multiphysical simulation of an NVO-based cathode. Normalized concentration of Zn ions inside the whole electrode containing an NVO cathode with a higher diffusion coefficient of 5×10^{-9} cm s^{-1} at (a) 10%, (b) 30%, (c) 50%, (d) 70%, and (e) 100% DoD (DoD = depth of discharge). Normalized concentration of Zn ions inside the whole electrode containing an NVO cathode with a lower diffusion coefficient of 5×10^{-11} cm s^{-1} at (f) 10%, (g) 30%, (h) 50%, (i) 75%, and (j) 100% DoD.

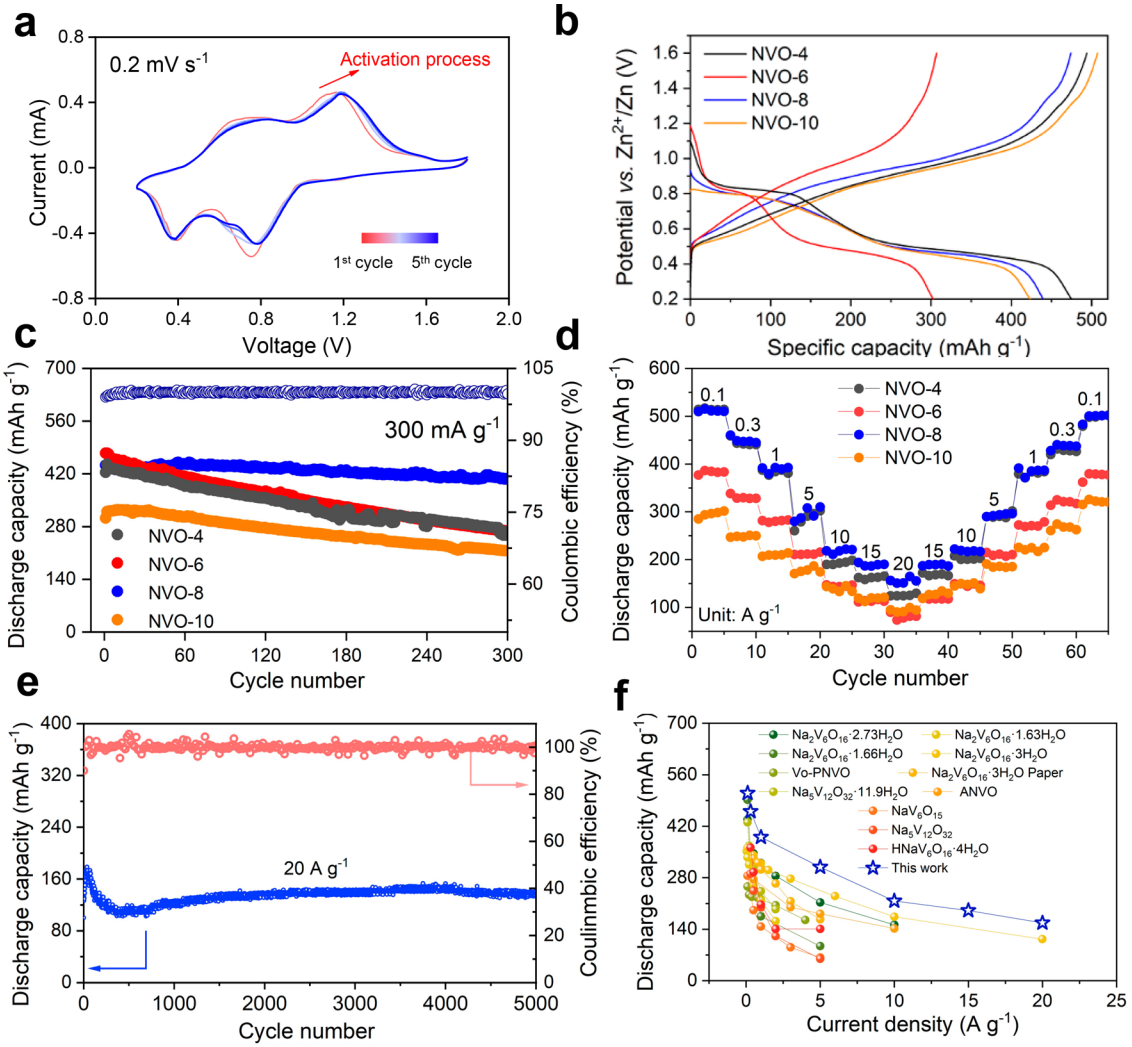

Figure 5. Electrochemical performance of textured NVO-8 cathode. (a) Cyclic voltammetry of textured NVO-8 at continuous cycles. (b) Initial voltage profiles of different NVO cathodes and (c) corresponding cyclic performance at the current density of 300 mA g^{-1}. (d) Rate capability of different NVO cathodes. (e) Cyclic performance of textured NVO-8 cathode at a current density of 10 A g^{-1}. (f) Comparison of the electrochemical performances from the available vanadium-based cathodes and textured NVO-8 in this work.

hydrogen peroxide exhibits a higher diffusion coefficient in NVO-8 compared with the other samples, which can be regarded as the explanation for the outstanding electrochemical kinetics. It is widely accepted that the polarization of electrodes, especially at higher current density, is determined by the electrochemical kinetics through the concentration field and the associated electric field, which affect the rate capacity directly. Therefore, a multiphysics

https://doi.org/10.1021/acsenergylett.2c01890
ACS Energy Lett. 2022, 7, 3770−3779

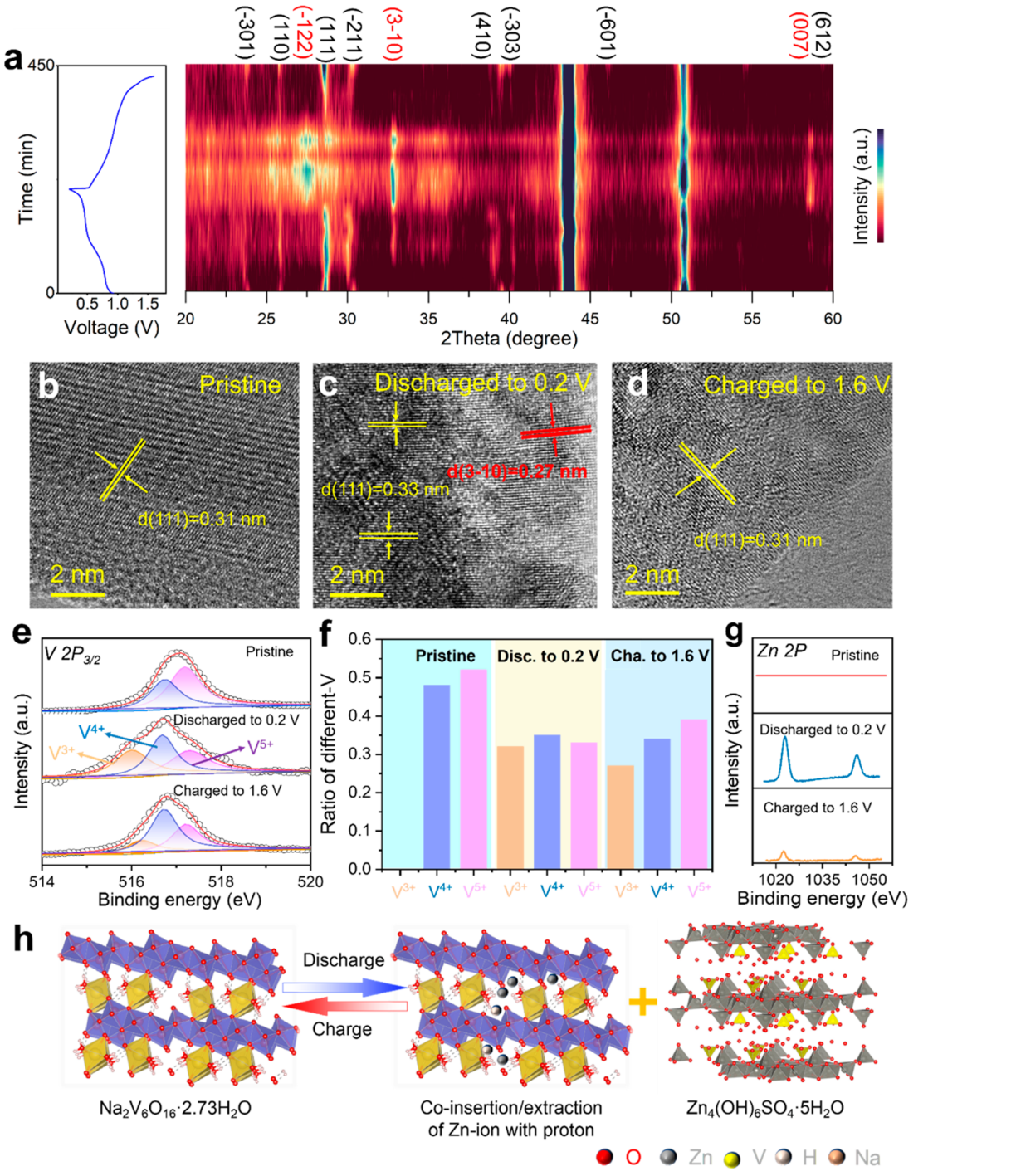

Figure 6. Mechanism of textured NVO-8 as cathode for AZIBs. (a) Voltage profile of textured NVO-8 during the discharge/charge process ranging from 0.2 to 1.6 V and the corresponding in situ XRD contour plots. High-resolution TEM image of the NVO-8 cathode (b) pristine, (c) discharged to 0.2 V, and (d) charged to 1.6 V. (e) High-resolution XPS of V $2p_{2/3}$ and (f) the corresponding ratio of different-valence vanadium of the NVO-8 cathode at different stages. (g) Zn 2*p* spectra of the NVO-8 cathode at different stages. (h) Schematic diagram of the mechanism of NVO-8 as cathode for AZIBs.

simulation was conducted to visualize the concentration distribution of Zn ions during electrochemical reaction in an NVO-based electrode. As shown in Figure S13, the size of NVO nanobelts inside the electrode generated with random function based on the Gaussian distribution is concentrated at 1000 × 150 × 20 nm, which is consistent with the morphology of the NVO from the SEM image. Meanwhile, the spatial distribution of the generated NVO nanobelts is a random arrangement with the relative parallel. An obvious concentration of Zn ions appears on the interface of the electrode containing the textured NVO-8 with a diffusion coefficient of 5 × 10^{-9} cm s^{-1} against the electrolyte at the depth of discharge (DoD) of 10% (Figure 4a), which increases well with discharge processes to DoD = 50% (Figure 4b,c and Figure S14a). Nevertheless, the concentration of Zn ions increases at the early discharge stage of DoD = 10% when the diffusion coefficient of Zn ion is lower by 2 orders of magnitude, at 5 × 10^{-11} cm s^{-1}; even at DoD = 50%, the insertion of Zn ions

https://doi.org/10.1021/acsenergylett.2c01890
ACS Energy Lett. 2022, 7, 3770−3779

inside the electrode is still relatively lower than that with a higher diffusion coefficient (Figure 4f–h and Figure S14c). At the final discharge stage of DoD = 100%, the concentration of Zn ions inside the whole electrode with textured NVO is not only higher but also more even than that with other NVO cathodes with sluggish diffusion of Zn ions (Figure 4d,e and i,j). In contrast, the cross-sectional distribution of Zn ions in the NVO cathode at the position of $Z = 1.5$ μm was shifted, as shown in Figure S15. Insertion of the Zn ions first occurs at the surface of each NVO nanobelt and develops into the center gradually. Eventually, the insertion uniformity of Zn ions into the textured NVO cathode with a higher diffusion coefficient is enhanced, compared to that in the NVO cathode with the lower diffusion coefficient (Figure S16). Therefore, the above results solidly suggested that the fast diffusion of Zn ions inside the textured NVO-8 cathode was the guarantee for uniformity of inside concentration field with lower polarization, predicting the great capacity delivered by textured NVO-8. As shown in the results from the multiphysics simulation mentioned above, the lowered polarization of the NVO electrode due to the uniform concentration field of Zn ions and electric field inside the electrode is guaranteed by the reinforced electrochemical kinetics from the special texture of NVO-8, promising the enhanced electrochemical performance.

Therefore, the as-prepared NVO cathodes were coupled with polished Zn metal as anode, 2 M $ZnSO_4$ electrolyte, and 0.4 M Na_2SO_4 as an additive to evaluate the electrochemical performance. First, cyclic voltammetry was carried out at a low scanning rate of 0.2 mV s^{-1} to follow the electrochemical reaction adequately (Figure 5a). As shown in the initial cycle, two reduction peaks located at 0.79 and 0.41 V are obvious, which can be explained as the electrochemical intercalation of Zn ions into the layer structure along with the reduction of V(+4) and V(+5) to lower valences.[49] Meanwhile, two oxidation peaks appear at 0.68 and 0.92 V, indicating the de-intercalation of Zn ions from the interlayer space.[50] A slight shift of CV curves in subsequent cycles can be explained as the result of the activation process for the fresh NVO electrode, and the great reproducibility of CV curves for the following cycles is closely related to the electrochemical reversibility of the NVO-8 cathode. Comparatively, the reduction and oxidation peaks with different intensities are exhibited in similar spots on the CV curves for other NVO cathodes (Figure S17). Furthermore, the galvanostatic discharge and charge process was conducted to uncover the improved capability of the as-prepared textured NVO-8 cathode. As shown in Figure 5b, the distinct plateaus of the discharge and charge process are consistent with the spots of the peaks for the electrochemical reactions of the CV curves. Moreover, the initial discharge capacity of the textured NVO-8 cathode is 443.2 mAh g^{-1}, much improved compared with the capacities of 302.6 and 424.2 mAh g^{-1} for NVO-6 and NVO-10, respectively. It should be noticed that the textured NVO-8 also delivers ultra-stable cyclic performance, exhibiting 401.1 mAh g^{-1} after 300 cycles, with the highest retention rate of 91.8% (Figure 5c). Regardless of the initial capacity of 475.1 mAh g^{-1}, NVO-4 maintains only 267.8 mAh g^{-1} after 300 cycles, with the highest capacity fading of 43.8%, compared with those of 33.3% and 39.4% for NVO-6 and NVO-10, respectively. Along with repeated cycling, polarization inside the NVO-8 cell holds fairly steady, whereas those of the others degrade obviously (Figure S18).

Practically, high-rate performance is the vital criterion of AZIBs for grid energy storage applications. As illustrated above, the great rate capacity and stability of the NVO-8 cathode can be predicted reasonably due to the fostered fast kinetics diffusion of Zn ions. A series of current densities were applied to examine the rate performance of textured NVO-8 cathodes, which delivered rate capacities of 510.0, 460.6, 390.7, 309.9, 217.7, 191.5, and 156.9 mAh g^{-1} at surging current densities of 0.1, 0.3, 1, 5, 10, 15, and 20 A g^{-1}, respectively (Figure 5d). When the applied current densities go back to the lower level from the ultra-high current density of 20 to 0.1 A g^{-1}, the NVO-8 delivers capacities of 187.3, 222.3, 290.1, 391.7, 428.2, and 500.6 mAh g^{-1} from 15 to 0.1 A g^{-1} with great reversibility. Furthermore, the AZIBs with textured NVO-8 were cycled at 20 A g^{-1} to verify the cycling stability under high current density. As could be observed in Figure 5e, the capacity increases rapidly from the initial value of 122.2 to 179.8 mAh g^{-1} after an activation process and could still maintain a capacity of 140.6 mAh g^{-1} after 5000 cycles, allowing a mild fading of 0.004% capacity per cycle. The intensively demonstrated great rate performance of the textured NVO-8 cathode herein can be attributed to the reinforced diffusion of Zn ions through crystal engineering. Finally, as shown in Figure 5f and Table S1, by comparison with other sodium vanadate cathode materials for AZIBs,[30,33−35,38,46,51−54] the NVO-8 cathode exhibits remarkable superiority.

In order to clarify the mechanism during charge/discharge of the NVO-8 cathode, in situ XRD was selected together with cycling at the current density of 100 mA g^{-1} within the voltage range from 0.2 to 1.6 V, as shown in Figure 6a. The XRD pattern at the first scanning is indexed well with that of the as-prepared NVO-8 cathode (Figure S19). The diffraction peaks at 24.03, 25.80, 25.58, 30.59, 38.78, 39.67, 45.52, and 59.62° of this initial XRD pattern correspond to the (−301), (110), (111), (−211), (410), (−303), (−601), and (612) crystal planes of the textured NVO-8 cathode, respectively. Along with discharge to 0.7 V, new peaks appeared at 32.83° and 59.22°, which were attributed to the (3−10) and (007) crystal planes of basic zinc sulfate pentahydrate ($Zn_4(OH)_6SO_4\cdot 5H_2O$) (PDF#39-0688),[55,56] with intensities increasing gradually with a drop in voltage, directly weakening the signals of the characteristic peaks of NVO-8. When the current is reversed, the higher-angle-shifted peaks of textured NVO-8 gradually relax to the initial stage and the peak of $Zn_4(OH)_6SO_4\cdot 5H_2O$ tends to weaken after charging back to 0.8 V. More specifically, the appearance of $Zn_4(OH)_6SO_4\cdot 5H_2O$, a hydroxide byproduct resulting from the change in local pH of the electrolyte during the charge/discharge process, is considered evidence of co-insertion and co-extraction of protons and Zn ions during the reaction.

In addition, the structural change of textured NVO-8 cathode after being discharged to 0.2 V and charged back to 1.6 V was revealed by HRTEM analysis, as shown in Figure 6b–d. The interplanar spacing is widened from 0.31 nm at the pristine stage to 0.33 nm at 0.2 V. Meanwhile, the edge of discharged NVO-8 was covered by the gray-white (3−10) plane of $Zn_4(OH)_6SO_4\cdot 5H_2O$, identical with the previous observations. When the NVO-8 is charged back to 1.6 V, the widened interplanar spacing returns to 0.31 nm, corresponding to the characteristic facet of NVO-8. This result indicates the high reversibility of lattice structure upon cycling for the NVO-8 cathode, which was confirmed by the XRD patterns and

https://doi.org/10.1021/acsenergylett.2c01890
ACS Energy Lett. 2022, 7, 3770−3779

element mapping at different cyclic stages as well (Figures S19 and S20). Furthermore, XPS was conducted to uncover the chemical state of the textured NVO-8 surface at different charge and discharge states. As shown in Figure 6e, V $2p_{3/2}$ is assigned to two signal peaks located at 516.8 and 517.4 eV, which were assigned to V(+4) and V(+5), respectively.[57,58] When discharged to 0.2 V, a new peak appeared at 515.8 eV, which can be attributed to V(+3), indicating that high-state V ions were reduced with the co-insertion of Zn ions and protons. However, when the NVO-8 cathode was charged to 1.6 V, V(+3) was oxidized to V(+4) and V(+5) successively during the extraction of Zn ions and protons. In order to explain the change of V valence more intuitively, the ratio of different valences of V is presented in Figure 6f for different voltage states. In addition, the Zn 2*p* was found at a deep discharge state with high intensity (Figure 6g), remaining a weak signal when charged to 1.6 V, which can be attributed to the residual $Zn_4(OH)_6SO_4{\cdot}5H_2O$ according to the in situ XRD analysis.[59] Thus, the co-insertion and co-extraction of Zn ions with protons accompanied by the generation of $Zn_4(OH)_6SO_4{\cdot}5H_2O$ was revealed, and the schematic illustration in Figure 6h explains the electrochemical mechanism, highlighting that the advantage of the electrochemical mechanism of co-deintercalation of zinc ions and protons does not cause a reversible or irreversible phase transition of the NVO-8 cathode material.

To sum up, the textured NVO cathode was successfully designed by crystal engineering, which was guided by theoretical predictions. Based on the different pathways of Zn ions inside the NVO cathode, the tunnel in line was uncovered as the preferable migration pathway with a lower energy barrier, illustrating that the sample with plenty of active plane and $b \neq 0$ possesses a higher diffusion coefficient. Meanwhile, uniform distribution of the concentration field for Zn ions inside the textured NVO was obtained by the fostered electrochemical kinetics, which was solidly visualized through multiphysics simulation. Therefore, the promising electrochemical performance of AZIBs, especially the satisfying capacity of 156.9 mAh g^{-1} at the higher current density of 20 A g^{-1}, was exhibited with great long-term cycle vitality (a capacity of 140.6 mAh g^{-1} with retention of 78.5% after 5000 cycles). The crystal engineering revealed in this work can be proposed as an efficient strategy to improve the electrochemical performance of cathode materials fundamentally, even for lithium, sodium, and potassium ion batteries, etc.

■ ASSOCIATED CONTENT

Supporting Information

The Supporting Information is available free of charge at https://pubs.acs.org/doi/10.1021/acsenergylett.2c01890.

Calculation and experimental methods; TGA, XPS, SEM, and BET of as-prepared NVO; calculation of GITT; geometric model for phase-field modeling; CV curves of NVO full cells; charge/discharge voltage profiles of NVO full cells; and XRD patterns and element mapping of NVO cathode at different stages, including Figures S1−S20; Table S1 summarizing rate performance comparison between this work and the reported works (PDF)

■ AUTHOR INFORMATION

Corresponding Authors

Ying Bai − *International Joint Research Laboratory of New Energy Materials and Devices of Henan Province, School of Physics and Electronics, Academy for Advanced Interdisciplinary Studies, Henan University, Kaifeng 475004, P.R. China*; orcid.org/0000-0001-7835-7067; Email: ybai@henu.edu.cn

Yangyang Liu − *International Joint Research Laboratory of New Energy Materials and Devices of Henan Province, School of Physics and Electronics, Academy for Advanced Interdisciplinary Studies, Henan University, Kaifeng 475004, P.R. China; State Key Laboratory for Mechanical Behavior of Materials, Xi'an Jiaotong University, Xi'an 710049, P.R. China*; Email: liuyy0510@hotmail.com

Shizhao Xiong − *State Key Laboratory for Mechanical Behavior of Materials, Xi'an Jiaotong University, Xi'an 710049, P.R. China; Department of Physics, Chalmers University of Technology, SE 412 96 Göteborg, Sweden*; orcid.org/0000-0003-1795-7805; Email: shizhao.xiong@chalmers.se

Authors

Shijia Li − *International Joint Research Laboratory of New Energy Materials and Devices of Henan Province, School of Physics and Electronics, Academy for Advanced Interdisciplinary Studies, Henan University, Kaifeng 475004, P.R. China*

Xieyu Xu − *State Key Laboratory for Mechanical Behavior of Materials, Xi'an Jiaotong University, Xi'an 710049, P.R. China*

Kai Wang − *International Joint Research Laboratory of New Energy Materials and Devices of Henan Province, School of Physics and Electronics, Academy for Advanced Interdisciplinary Studies, Henan University, Kaifeng 475004, P.R. China*

Weixin Chen − *School of Materials, Sun Yat-sen University, Shenzhen 518107, P.R. China*

Xia Lu − *School of Materials, Sun Yat-sen University, Shenzhen 518107, P.R. China*; orcid.org/0000-0003-3504-9069

Zhongxiao Song − *State Key Laboratory for Mechanical Behavior of Materials, Xi'an Jiaotong University, Xi'an 710049, P.R. China*; orcid.org/0000-0002-7317-2343

Jang-Yeon Hwang − *Department of Materials Science and Engineering, Chonnam National University, Gwangju 500-757, South Korea*; orcid.org/0000-0003-3802-7439

Jaekook Kim − *Department of Materials Science and Engineering, Chonnam National University, Gwangju 500-757, South Korea*; orcid.org/0000-0002-6638-249X

Complete contact information is available at: https://pubs.acs.org/10.1021/acsenergylett.2c01890

Notes

The authors declare no competing financial interest.

■ ACKNOWLEDGMENTS

This work was supported by the National Natural Science Foundation of China (52072112, 51672069), the Zhong Yuan Thousand Talents Program of Henan Province (ZYQR201912155), the Henan Overseas Expertise Introduction Center for Discipline Innovation (CXJD2021003), the

Program for Innovative Research Team in Science and Technology in the University of Henan Province (20IRTSTHN012), the Science and Technology Development Project of Henan Province (202102210105, 192102210235), the National Natural Science Foundation of China (No. 51802256), and the China Scholarship Council (No. 201908090043). The authors thank the Chalmers Areas of Advance Materials Science and Energy for support.

REFERENCES

(1) Liu, Y.; Xu, X.; Kapitanova, O. O.; Evdokimov, P. V.; Song, Z.; Matic, A.; Xiong, S. Electro-Chemo-Mechanical Modeling of Artificial Solid Electrolyte Interphase to Enable Uniform Electrodeposition of Lithium Metal Anodes. *Adv. Energy Mater.* **2022**, *12* (9), 2103589.

(2) Liu, Y.; Xu, X.; Sadd, M.; Kapitanova, O. O.; Krivchenko, V. A.; Ban, J.; Wang, J.; Jiao, X.; Song, Z.; Song, J.; Xiong, S.; Matic, A. Insight into the Critical Role of Exchange Current Density on Electrodeposition Behavior of Lithium Metal. *Adv. Sci.* **2021**, *8* (5), 2003301.

(3) Xu, X.; Jiao, X.; Kapitanova, O. O.; Wang, J.; Volkov, V. S.; Liu, Y.; Xiong, S. Diffusion Limited Current Density: A Watershed in Electrodeposition of Lithium Metal Anode. *Adv. Energy Mater.* **2022**, *12* (19), 2200244.

(4) Xu, X.; Liu, Y.; Hwang, J. Y.; Kapitanova, O. O.; Song, Z.; Sun, Y. K.; Matic, A.; Xiong, S. Role of Li-Ion Depletion on Electrode Surface: Underlying Mechanism for Electrodeposition Behavior of Lithium Metal Anode. *Adv. Energy Mater.* **2020**, *10* (44), 2002390.

(5) Liu, Q.; Su, X.; Lei, D.; Qin, Y.; Wen, J.; Guo, F.; Wu, Y. A.; Rong, Y.; Kou, R.; Xiao, X.; Aguesse, F.; Bareño, J.; Ren, Y.; Lu, W.; Li, Y. Approaching the capacity limit of lithium cobalt oxide in lithium ion batteries via lanthanum and aluminium doping. *Nat. Energy* **2018**, *3* (11), 936−943.

(6) Xu, G.-L.; Liu, Q.; Lau, K. K. S.; Liu, Y.; Liu, X.; Gao, H.; Zhou, X.; Zhuang, M.; Ren, Y.; Li, J.; Shao, M.; Ouyang, M.; Pan, F.; Chen, Z.; Amine, K.; Chen, G. Building ultraconformal protective layers on both secondary and primary particles of layered lithium transition metal oxide cathodes. *Nat. Energy* **2019**, *4* (6), 484−494.

(7) Li, Q.; Rui, X.; Chen, D.; Feng, Y.; Xiao, N.; Gan, L.; Zhang, Q.; Yu, Y.; Huang, S. A High-Capacity Ammonium Vanadate Cathode for Zinc-Ion Battery. *Nanomicro Lett.* **2020**, *12* (1), 67.

(8) Deng, W.; Zhou, Z.; Li, Y.; Zhang, M.; Yuan, X.; Hu, J.; Li, Z.; Li, C.; Li, R. High-Capacity Layered Magnesium Vanadate with Concentrated Gel Electrolyte toward High-Performance and Wide-Temperature Zinc-Ion Battery. *ACS Nano* **2020**, *14* (11), 15776−15785.

(9) Wang, L.; Liu, T.; Wu, T.; Lu, J. Exploring new battery knowledge by advanced characterizing technologies. *Exploration* **2021**, *1* (3), 20210130.

(10) Wei, T.; Liu, Y.; Yang, G.; Wang, C. Aluminum vanadate hollow spheres as zero-strain cathode material for highly reversible and durable aqueous zinc-ion batteries. *Energy Storage Mater.* **2020**, *30*, 130−137.

(11) Xu, X.; Liu, Y.; Kapitanova, O. O.; Song, Z.; Sun, J.; Xiong, S. Electro-chemo-mechanical failure of solid electrolyte induced by growth of internal lithium filaments. *Adv. Mater.* **2022**, e2207232.

(12) Zhou, W.; Chen, J.; Chen, M.; Wang, A.; Huang, A.; Xu, X.; Xu, J.; Wong, C.-P. An environmentally adaptive quasi-solid-state zinc-ion battery based on magnesium vanadate hydrate with commercial-level mass loading and anti-freezing gel electrolyte. *J. Mater. Chem. A* **2020**, *8* (17), 8397−8409.

(13) Guo, S.; Qin, L.; Zhang, T.; Zhou, M.; Zhou, J.; Fang, G.; Liang, S. Fundamentals and perspectives of electrolyte additives for aqueous zinc-ion batteries. *Energy Storage Mater.* **2021**, *34*, 545−562.

(14) Zhang, N.; Chen, X.; Yu, M.; Niu, Z.; Cheng, F.; Chen, J. Materials chemistry for rechargeable zinc-ion batteries. *Chem. Soc. Rev.* **2020**, *49* (13), 4203−4219.

(15) Yang, K.; Ying, Y.; Cui, L.; Sun, J.; Luo, H.; Hu, Y.; Zhao, J. Stable aqueous Zn−Ag and Zn−polyoxometalate hybrid battery driven by successive Ag+ cation and polyoxoanion redox reactions. *Energy Storage Mater.* **2021**, *34*, 203−210.

(16) Tang, W.; Lan, B.; Tang, C.; An, Q.; Chen, L.; Zhang, W.; Zuo, C.; Dong, S.; Luo, P. Urchin-like Spinel MgV2O4 as a Cathode Material for Aqueous Zinc-Ion Batteries. *ACS Sustainable Chem. Eng.* **2020**, *8* (9), 3681−3688.

(17) Wang, X.; Xi, B.; Ma, X.; Feng, Z.; Jia, Y.; Feng, J.; Qian, Y.; Xiong, S. Boosting Zinc-Ion Storage Capability by Effectively Suppressing Vanadium Dissolution Based on Robust Layered Barium Vanadate. *Nano Lett.* **2020**, *20* (4), 2899−2906.

(18) Xu, C.; Li, B.; Du, H.; Kang, F. Energetic zinc ion chemistry: the rechargeable zinc ion battery. *Angew. Chem., Int. Ed. Engl.* **2012**, *51* (4), 933−5.

(19) Alfaruqi, M. H.; Mathew, V.; Gim, J.; Kim, S.; Song, J.; Baboo, J. P.; Choi, S. H.; Kim, J. Electrochemically Induced Structural Transformation in a γ-MnO2Cathode of a High Capacity Zinc-Ion Battery System. *Chem. Mater.* **2015**, *27* (10), 3609−3620.

(20) Alfaruqi, M. H.; Gim, J.; Kim, S.; Song, J.; Jo, J.; Kim, S.; Mathew, V.; Kim, J. Enhanced reversible divalent zinc storage in a structurally stable α-MnO 2 nanorod electrode. *J. Power Sources* **2015**, *288*, 320−327.

(21) Lee, J.; Ju, J. B.; Cho, W. I.; Cho, B. W.; Oh, S. H. Todorokite-type MnO2 as a zinc-ion intercalating material. *Electrochim. Acta* **2013**, *112*, 138−143.

(22) Chuai, M.; Yang, J.; Wang, M.; Yuan, Y.; Liu, Z.; Xu, Y.; Yin, Y.; Sun, J.; Zheng, X.; Chen, N.; Chen, W. High-performance Zn battery with transition metal ions co-regulated electrolytic MnO2. *eScience* **2021**, *1* (2), 178−185.

(23) Liu, Z.; Pulletikurthi, G.; Endres, F. A Prussian Blue/Zinc Secondary Battery with a Bio-Ionic Liquid-Water Mixture as Electrolyte. *ACS Appl. Mater. Interfaces* **2016**, *8* (19), 12158−64.

(24) Zhang, L.; Chen, L.; Zhou, X.; Liu, Z. Morphology-Dependent Electrochemical Performance of Zinc Hexacyanoferrate Cathode for Zinc-Ion Battery. *Sci. Rep.* **2015**, *5*, 18263.

(25) Hou, Z.; Zhang, X.; Li, X.; Zhu, Y.; Liang, J.; Qian, Y. Surfactant widens the electrochemical window of an aqueous electrolyte for better rechargeable aqueous sodium/zinc battery. *J. Mater. Chem. A* **2017**, *5* (2), 730−738.

(26) Liu, C.; Neale, Z.; Zheng, J.; Jia, X.; Huang, J.; Yan, M.; Tian, M.; Wang, M.; Yang, J.; Cao, G. Expanded hydrated vanadate for high-performance aqueous zinc-ion batteries. *Energy Environ. Sci.* **2019**, *12* (7), 2273−2285.

(27) Zhang, X.; Hu, J. P.; Fu, N.; Zhou, W. B.; Liu, B.; Deng, Q.; Wu, X. W. Comprehensive review on zinc-ion battery anode: Challenges and strategies. *InfoMat* **2022**, *4* (7), e12306.

(28) Wu, Y.; Song, T.-Y.; Chen, L.-N. A review on recent developments of vanadium-based cathode for rechargeable zinc-ion batteries. *Tungsten* **2021**, *3* (3), 289−304.

(29) Fegade, U.; Jethave, G.; Khan, F.; Al-Ahmed, A.; Karmouch, R.; Shariq, M.; Inamuddin; Ahmer, M. F. Recent development of aqueous zinc-ion battery cathodes and future challenges: Review. *Int. J. Energy Res.* **2022**, *46* (10), 13152−13177.

(30) Tan, H.; Chen, D.; Liu, W.; Liu, C.; Lu, B.; Rui, X.; Yan, Q. Free-Standing Hydrated Sodium Vanadate Papers for High-Stability Zinc-Ion Batteries. *Batteries Supercaps* **2020**, *3* (3), 254−260.

(31) Wang, H.; Wang, W.; Ren, Y.; Huang, K.; Liu, S. A new cathode material $Na_2V_6O_{16}{\cdot}xH_2O$ nanowire for lithium ion battery. *J. Power Sources* **2012**, *199*, 263−269.

(32) Zhang, W.; Xu, G.; Yang, L.; Ding, J. Ultra-long $Na_2V_6O_{16}{\cdot}xH_2O$ nanowires: large-scale synthesis and application in binder-free flexible cathodes for lithium ion batteries. *RSC Adv.* **2016**, *6* (7), 5161−5168.

(33) Hu, F.; Xie, D.; Zhao, D.; Song, G.; Zhu, K. $Na_2V_6O_{16}{\cdot}2.14H_2O$ nanobelts as a stable cathode for aqueous zinc-ion batteries with long-term cycling performance. *J. Energy Chem.* **2019**, *38*, 185−191.

(34) Qin, L.; Li, S.; Li, L.; Fang, G.; Cheng, H.; Zhu, Q.; Gao, H.; Chen, S. Improved working voltage and high rate performance of sodium vanadate cathode materials for aqueous zinc ion batteries by

https://doi.org/10.1021/acsenergylett.2c01890
ACS Energy Lett. 2022, 7, 3770−3779

altering synthetic solution pH guiding the structure change. *Mater. Today Commun.* **2022**, *31*, 103460.
(35) Soundharrajan, V.; Sambandam, B.; Kim, S.; Alfaruqi, M. H.; Putro, D. Y.; Jo, J.; Kim, S.; Mathew, V.; Sun, Y. K.; Kim, J. $Na_2V_6O_{16}.3H_2O$ Barnesite Nanorod: An Open Door to Display a Stable and High Energy for Aqueous Rechargeable Zn-Ion Batteries as Cathodes. *Nano Lett.* **2018**, *18* (4), 2402−2410.
(36) Sambandam, B.; Soundharrajan, V.; Kim, S.; Alfaruqi, M. H.; Jo, J.; Kim, S.; Mathew, V.; Sun, Y.-k.; Kim, J. $K_2V_6O_{16}{\cdot}2.7H_2O$ nanorod cathode: an advanced intercalation system for high energy aqueous rechargeable Zn-ion batteries. *J. Mater. Chem. A* **2018**, *6* (32), 15530−15539.
(37) Li, Z.; Lv, L.; Pei, J.; Kong, S.; Li, L.; Zhang, S. A self-standing $CaV_6O_{16}{\cdot}3H_2O$ paper electrode for lithium-ion batteries. *Mater. Lett.* **2021**, *299*, 130094.
(38) Guo, X.; Fang, G.; Zhang, W.; Zhou, J.; Shan, L.; Wang, L.; Wang, C.; Lin, T.; Tang, Y.; Liang, S. Mechanistic Insights of Zn^{2+} Storage in Sodium Vanadates. *Adv. Energy Mater.* **2018**, *8* (27), 1801819.
(39) Li, S.; Yang, X.; Li, X.; Wei, Z.; Li, M.; Hu, F.; Xie, Y.; Meng, X.; Wang, C.; Chen, G.; Du, F. Aqueous nickel-ion battery with $Na_2V_6O_{16}{\cdot}2H_2O$ nanowire as high-capacity and zero-strain host material. *Chem. Eng. J.* **2021**, *413*, 127441.
(40) Zhou, M.; Guo, S.; Li, J.; Luo, X.; Liu, Z.; Zhang, T.; Cao, X.; Long, M.; Lu, B.; Pan, A.; Fang, G.; Zhou, J.; Liang, S. Surface-Preferred Crystal Plane for a Stable and Reversible Zinc Anode. *Adv. Mater.* **2021**, *33* (21), e2100187.
(41) Liu, Y.; Xiong, S.; Deng, J.; Jiao, X.; Song, B.; Matic, A.; Song, J. Stable Li metal anode by crystallographically oriented plating through in-situ surface doping. *Sci. China Mater.* **2020**, *63* (6), 1036−1045.
(42) Wu, Z.; Ye, F.; Liu, Q.; Pang, R.; Liu, Y.; Jiang, L.; Tang, Z.; Hu, L. Simultaneous Incorporation of V and Mn Element into Polyanionic NASICON for High Energy-Density and Long-Lifespan Zn-Ion Storage. *Adv. Energy Mater.* **2022**, *12* (23), 2200654.
(43) Sun, R.; Ji, X.; Luo, C.; Hou, S.; Hu, P.; Pu, X.; Cao, L.; Mai, L.; Wang, C. Water-Pillared Sodium Vanadium Bronze Nanowires for Enhanced Rechargeable Magnesium Ion Storage. *Small* **2020**, *16* (30), e2000741.
(44) Wan, F.; Zhang, L.; Dai, X.; Wang, X.; Niu, Z.; Chen, J. Aqueous rechargeable zinc/sodium vanadate batteries with enhanced performance from simultaneous insertion of dual carriers. *Nat. Commun.* **2018**, *9* (1), 1656.
(45) Jo, J. H.; Aniskevich, Y.; Kim, J.; Choi, J. U.; Kim, H. J.; Jung, Y. H.; Ahn, D.; Jeon, T. Y.; Lee, K. S.; Song, S. H.; Kim, H.; Ragoisha, G.; Mazanik, A.; Streltsov, E.; Myung, S. T. New Insight on Open-Structured Sodium Vanadium Oxide as High-Capacity and Long Life Cathode for Zn−Ion Storage: Structure, Electrochemistry, and First-Principles Calculation. *Adv. Energy Mater.* **2020**, *10* (40), 2001595.
(46) Hu, P.; Zhu, T.; Wang, X.; Wei, X.; Yan, M.; Li, J.; Luo, W.; Yang, W.; Zhang, W.; Zhou, L.; Zhou, Z.; Mai, L. Highly Durable $Na_2V_6O_{16}.1.63H_2O$ Nanowire Cathode for Aqueous Zinc-Ion Battery. *Nano Lett.* **2018**, *18* (3), 1758−1763.
(47) Qiu, M.; Jia, H.; Lan, C.; Liu, H.; Fu, S. An enhanced kinetics and ultra-stable zinc electrode by functionalized boron nitride intermediate layer engineering. *Energy Storage Mater.* **2022**, *45*, 1175−1182.
(48) Yang, K.; Hu, Y.; Li, L.; Cui, L.; He, L.; Wang, S.; Zhao, J.; Song, Y.-F. First high-nuclearity mixed-valence polyoxometalate with hierarchical interconnected Zn^{2+} migration channels as an advanced cathode material in aqueous zinc-ion battery. *Nano Energy* **2020**, *74*, 104851.
(49) Tang, C. R.; Singh, G.; Housel, L. M.; Kim, S. J.; Quilty, C. D.; Zhu, Y.; Wang, L.; Takeuchi, K. J.; Takeuchi, E. S.; Marschilok, A. C. Impact of sodium vanadium oxide (NaV_3O_8, NVO) material synthesis conditions on charge storage mechanism in Zn-ion aqueous batteries. *Phys. Chem. Chem. Phys.* **2021**, *23* (14), 8607−8617.
(50) Xu, N.; Lian, X.; Huang, H.; Ma, Y.; Li, L.; Peng, S. $CaV_6O_{16}{\cdot}3H_2O$ nanorods as cathode for high-performance aqueous zinc-ion battery. *Mater. Lett.* **2021**, *287*, 129285.
(51) Bi, W.; Gao, G.; Wu, G.; Atif, M.; AlSalhi, M. S.; Cao, G. Sodium vanadate/PEDOT nanocables rich with oxygen vacancies for high energy conversion efficiency zinc ion batteries. *Energy Storage Mater.* **2021**, *40*, 209−218.
(52) Yu, H.; Aakyiir, M.; Xu, S.; Whittle, J. D.; Losic, D.; Ma, J. Maximized crystal water content and charge-shielding effect in layered vanadate render superior aqueous zinc-ion battery. *Mater. Today Energy* **2021**, *21*, 100757.
(53) Liu, X.; Hu, X.; Hou, S.; He, W.; Liang, Z.; Meng, L.; Guo, Q.; Liu, T.; Ru, Q.; Zhao, L. Anion deficiency motivated $Na_2V_6O_{16}$ nanobelts for superior sustainable zinc ion storage. *J. Mater. Chem. A* **2021**, *9* (37), 21209−21218.
(54) Ran, Y.; Ren, J.; Yang, Z.; Wang, B.; Wang, Y. Preparation of NaV_6O_{15} Nanosheet Cathodes with High Cycling Performance and Good Capacity Retention Rate in Aqueous Zinc-Ion Batteries. *Phys. Status Solidi (a)* **2022**, *219* (9), 2100789.
(55) Zhao, S.; Han, B.; Zhang, D.; Huang, Q.; Xiao, L.; Chen, L.; Ivey, D. G.; Deng, Y.; Wei, W. Unravelling the reaction chemistry and degradation mechanism in aqueous Zn/MnO_2 rechargeable batteries. *J. Mater. Chem. A* **2018**, *6* (14), 5733−5739.
(56) Li, C.; Chi, X.; Huang, J.; Wu, J.; Liu, Y. Reversible Transformation of a Zinc Salt-Boosted High Areal Capacity Manganese Dioxide Cathode for Energy-Dense and Stable Aqueous Zinc Batteries. *ACS Appl. Energy Mater.* **2022**, *5* (2), 1478−1486.
(57) Zhu, K.; Wei, S.; Shou, H.; Shen, F.; Chen, S.; Zhang, P.; Wang, C.; Cao, Y.; Guo, X.; Luo, M.; Zhang, H.; Ye, B.; Wu, X.; He, L.; Song, L. Defect engineering on V_2O_3 cathode for long-cycling aqueous zinc metal batteries. *Nat. Commun.* **2021**, *12* (1), 6878.
(58) Wang, Z.; Zhou, M.; Qin, L.; Chen, M.; Chen, Z.; Guo, S.; Wang, L.; Fang, G.; Liang, S. Simultaneous regulation of cations and anions in an electrolyte for high-capacity, high-stability aqueous zinc−vanadium batteries. *eScience* **2022**, *2* (2), 209−218.
(59) Li, Z.; Ganapathy, S.; Xu, Y.; Zhou, Z.; Sarilar, M.; Wagemaker, M. Mechanistic Insight into the Electrochemical Performance of $ZnVO_2$ Batteries with an Aqueous $ZnSO_4$ Electrolyte. *Adv. Energy Mater.* **2019**, *9* (22), 1900237.

https://doi.org/10.1021/acsenergylett.2c01890
ACS Energy Lett. 2022, 7, 3770−3779